Source Estimation from Broadband Regional Seismograms

by Lian-She Zhao* and Donald V. Helmberger

Abstract Recently developed source inversion techniques do not take full advantage of the broadband nature of regional seismograms. The reason is that Green's functions generated from flat-layered models are not correct for the complicated propagational phenomena associated with realistic crustal structure. The inversion is usually performed by removing short periods and inverting only selected portions of the records. In this article, we introduce a source estimation technique that allows for better use of the entire broadband record when only imperfect Green's function are available. The procedure desensitizes the timing between the principal crustal arrivals by fitting portions of the Green's functions independently. The preferred source is the orientation that minimizes the average L1 and L2 norms in term of the four parameters, M_0, strike, dip, and rake. The L2 error emphasizes the longer period surface waves while the L1 error weights the shorter period body waves. We obtain estimates of duration by modeling long period and broadband signals. The depth determination can be obtained directly from the surface reflected phases sP_mP or sS_mS or by cycling through the depth-dependent Green's functions. In addition to the source parameters, we obtain "δt" phase alignments shifts that can be used as Green's function corrections for relocating other events or as a guide to deriving new crustal models.

Introduction

Recent studies of broadband data produced by modern instrumentation are generating considerable excitement in seismology (Kanamori et al., 1992). Regional observations are particularly interesting because of the broadband nature of crustal arrivals and the ability to compare mainshock and aftershock sequences. Typical examples from the TERRAscope array (Table 1) are displayed in Figures 1 and 2. The first is from the Sierra Madre event, which occurred in the middle of the array (see Fig. 3), and the second is from the Yucca Mountain event, which is to the side. Note that the Yucca Mountain aftershock is about 30 times smaller than the main event. Because it occurred only 17 min after the main event, it occurs within the coda of the main event and is quite noisy. The Sierra Madre aftershock is 100 times smaller than the main event but occurred during a quieter time and is less noisy.

In Figures 1 and 2, the top panels of these observations are displayed in broadband displacement, whereas the bottom panels show the long-period-simulated responses. Note that the long-period responses of the mainshock and aftershock are quite similar, whereas the

broadband data can appear quite different, particularly for some components, such as for the radial motions at GSC in Figure 1. When these motions are plotted on a larger scale and in velocity, it becomes possible to identify individual crustal arrivals. For instance, the strongest high-frequency phase is actually sS_mS, while the earlier signal is S_mS on regional seismograms (see Helmberger et al., unpublished manuscript). Thus, a great deal of information about directivity and crustal structure can be obtained from this type of data. This is discussed in considerable detail in Zhao and Helmberger (1991) and Helmberger et al. (unpublished manuscript).

The greatest challenge in addressing this type of data

Table 1
Stations

	Location
GSC	(35.302°N, 116.805°W)
ISA	(35.643°N, 118.480°W)
PAS	(34.148°N, 118.172°W)
PFO	(33.609°N, 116.455°W)
SBC	(34.442°N, 119.713°W)
STA	(37.404°N, 122.175°W)
SVD	(34.104°N, 117.098°W)

*On leave from: Institute for Geophysics, The University of Texas at Austin, 8701 North MoPac Blvd., Austin, Texas 78759.

is separating the details of faulting from wave propagation. The higher the frequency the more difficult the task. However, the first step is to establish the source depth and orientation with inadequate knowledge about the crust and corresponding imperfect Green's functions. One approach to handling this difficulty is to remove the shorter period body wave and invert the long-period surface wave, at the 50 sec period, as discussed by Thio and Kanamori (1992). This proves effective when the event is large enough to be above the noise level and good azimuthal coverage is available. The 5- to 10-sec surface waves are generally stronger than the 50-sec waves but are more difficult to invert owing to waveform instability caused by lateral variation. For example, the three stations, GSC, PAS, and PFO (Fig. 3) are roughly at the same distance to the 28 June 1991 Sierra Madre earthquake, but an overlay of their records reveals con-

siderable shifts in surface wave timing (see Dreger and Helmberger, 1991).

Dreger and Helmberger (1993) solve this problem by excluding the surface waves and inverting the body-wave portion of the records for source parameters. This approach proves effective at the longer periods when the Green's functions are more forgiving as can be appreciated by examining Figure 4. The top traces display the long-period GSC data from the Sierra Madre event with synthetics generated from two slightly different models (see Table 2). The broadband comparison is displayed in the lower panel. The two columns on the left show the enlarged portion of the P_{nl} waves. The various numbers indicate the time shifts required to align the synthetics with the data. These values are established by cross-correlation. For example, the (1.1) number indicates that the synthetic Rayleigh waves are too fast by 1.1 sec, and the upper crust needs to be slower as in model SD. Reducing the shallow velocity structure also
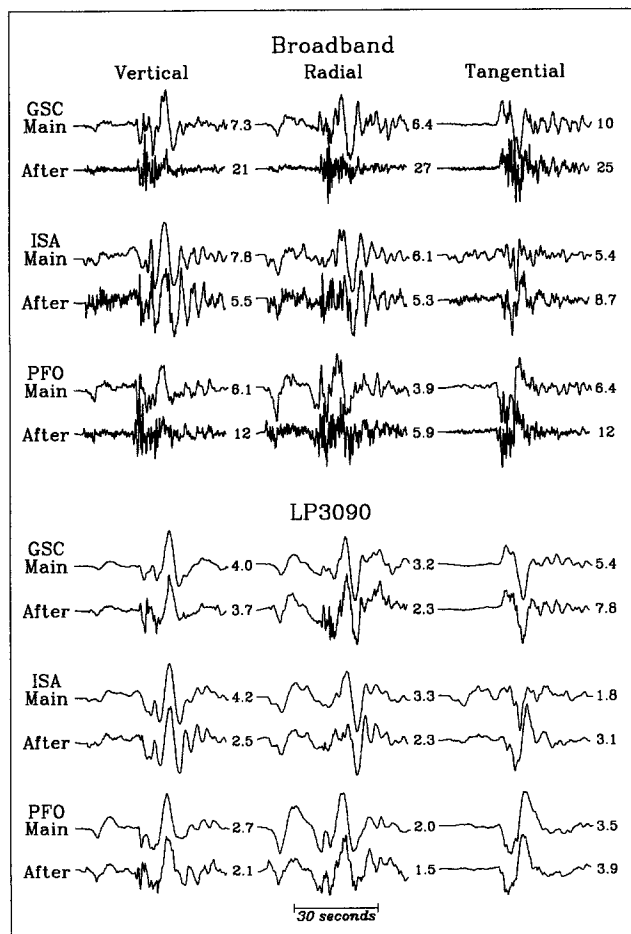

Figure 1. Regional broadband displacement of the Sierra Madre event along with those of an aftershock. Long-period bandpassed records are also given LP3090 (Press–Ewing), of which the gain used is 1. The numbers on the right of the seismograms are the amplitudes in centimeters. The scale of the amplitudes is 10^{-2} for the mainshock, 10^{-4} for the aftershock.
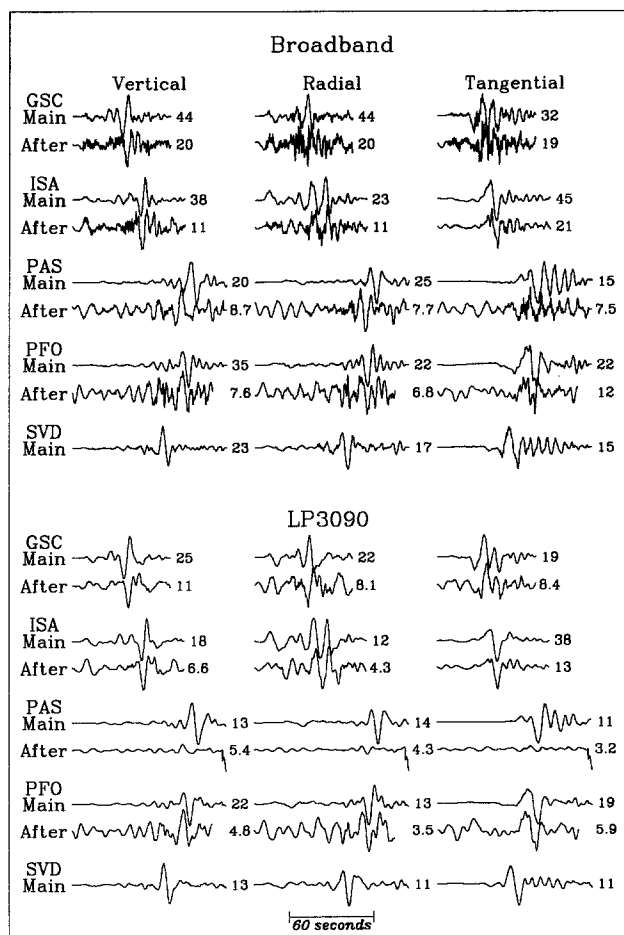

Figure 2. Regional broadband recordings of the Yucca Mountain event along with those of an aftershock. Long-period bandpassed records are also given LP3090 (Press–Ewing). The numbers on the right of the seismograms are the amplitudes in centimeters. The scale of the amplitudes is 10^{-3} for the mainshock, 10^{-4} for the aftershock.

increases the separation between the P_{nl} and S_mS phases and fits the body-wave data better as well. However, the slightly misaligned SC long-period synthetics still fit well enough to produce stable inversion results, and thus, the SC model can be used for many paths as discussed by Dreger and Helmberger (1993, unpublished manuscript).

Difficulty arises when attempting inversions at higher frequency, because a small shift in timing becomes significant. However, instead of fine tuning each individual path, for example, by changing model SC into SD, we can proceed by breaking up the seismograms into segments and searching for the best fit per section. This procedure not only provides accurate source parameter recovery but provides the "δt" shifts that can be used later in crustal structure studies.

The next section will discuss the method. This will be followed by application to a number of recent events showing the usefulness of this procedure in treating both main events and their aftershocks.

Computational Implementation

In the following, we use $f(t)$ and $g(t)$ as observed and synthetic seismograms, in which f and g can be any component. The synthetics can be calculated from:

$$g(t) = S(t) * \sum_{i=1}^{i=3} W_i(t)A_i(\Theta, \lambda, \delta)$$
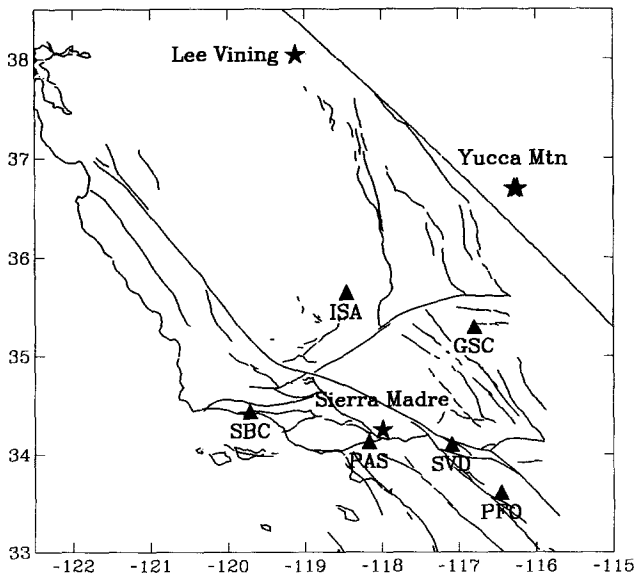
for vertical component,

Figure 3.   Map showing the present TERRA-scope stations (triangle), of which the coordinates are given in Table 1, and events (stars) considered in this study.

$$g(t) = S(t) * \sum_{i=1}^{i=3} Q_i(t)A_i(\Theta, \lambda, \delta)$$

for radial component,

and

$$g(t) = S(t) * \sum_{i=1}^{i=2} V_i(t)A_{i+3}(\Theta, \lambda, \delta)$$

for tangential component,   (1)

where $W_i(t)$, $Q_i(t)$, and $V_i(t)$ are the vertical, radial, and tangential Green's functions for the three fundamental faults, i.e., strike slip, dip slip, and 45° dip slip, at the appropriate distance and source depth respectively (e.g., Helmberger, 1983). $S(t)$ is the source time function. We assume that $S(t)$ is a trapezoid. The A_i contain the radiation pattern information of the source, namely,

$$A_1(\Theta, \lambda, \delta) = \sin2\Theta \cos\lambda \sin\delta$$
$$+ 0.5 \cos2\Theta \sin\lambda \sin2\delta,$$

$$A_2(\Theta, \lambda, \delta) = \cos\Theta \cos\lambda \cos\delta - \sin\Theta \sin\lambda \cos2\delta,$$

$$A_3(\Theta, \lambda, \delta) = 0.5 \sin\lambda \sin2\delta,$$

$$A_4(\Theta, \lambda, \delta) = \cos2\Theta \cos\lambda \sin\delta - 0.5 \sin2\Theta \sin\lambda \sin2\delta,$$

and

$$A_5(\Theta, \lambda, \delta) = -\sin\Theta \cos\lambda \cos\delta$$
$$- \cos\Theta \sin\lambda \cos2\delta,$$ (2)

are the functions of Θ, station azimuth from the source minus the fault strike θ, the fault dip δ, and the fault rake λ.

A relative time shift of the data $f(t)$ from the synthetics $g(t)$ can be estimated with the use of the cross-correlation function:

$$C(t) = \int_{-\infty}^{\infty} f(\tau)g(t + \tau)d\tau \Big/ \left(\int_{-\infty}^{\infty} f^2(\tau)d\tau \int_{-\infty}^{\infty} g^2(\tau)d\tau \right)^{1/2}.$$ (3)

The maximum of the positive values of $C(t)$ gives the largest cross-correlation coefficient, C_{fg}, for the best alignment of the data segment and corresponding synthetics. That is, the time, t, at which $C(t)$ reaches the maximum of the positive value.

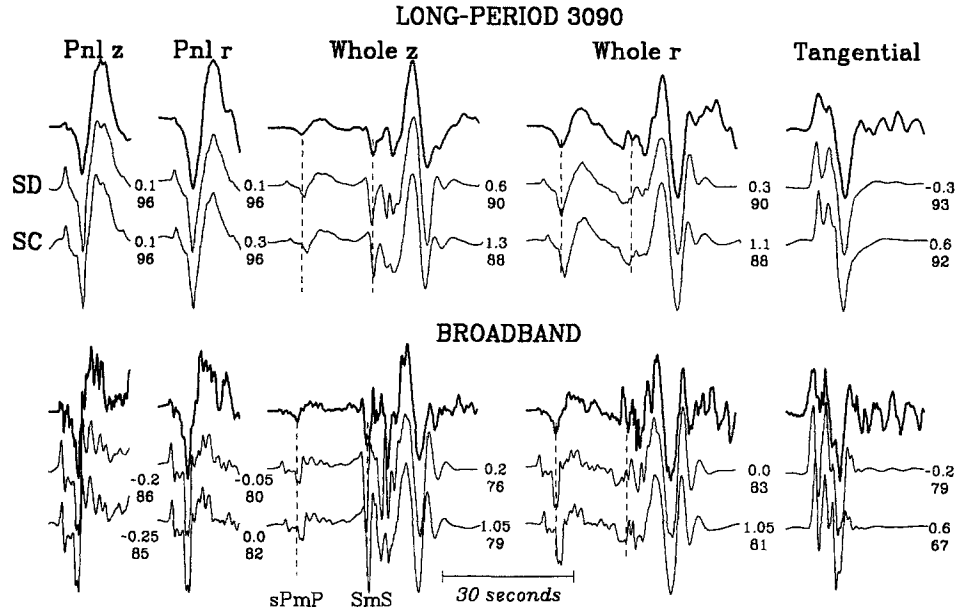The moment is the ratio of the peak amplitude of

Figure 4.   Synthetic comparisons of models SC and SD to the GSC long-period and broadband data of the Sierra Madre mainshock. The numbers on the right side of the seismograms are the time shifts (upper) and cross-correlation coefficient in percent (lower). The positive time shifts mean that the synthetics have been delayed or shifted to the right.

Table 2
Models

	SC				SD		
α	β	ρ	Thick	α	β	ρ	Thick
5.50	3.18	2.40	5.5	5.50	3.10	2.40	5.5
6.30	3.64	2.67	10.5	6.30	3.55	2.67	10.5
6.60	3.87	2.80	19.0	6.70	3.87	2.80	19.0
7.80	4.50	3.10	—	7.80	4.55	3.10	—

the data to that of the synthetics for the common time segment

$$M_0 = \text{Max}(|f(t)|)/\text{Max}(|g(t)|),   \quad (4)$$

if $g(t)$ is calculated without any reference moment.

The error estimation in this code involves both L1 and L2 norm. These norms are defined by

$$\text{L1}: \|f\| = \int_{t_1}^{t_2} |f(t)| dt,$$

and

$$\text{L2}: \|f\| = \int_{t_1}^{t_2} f(t) * f(t) dt,$$

where $[t_1, t_2]$ is the time interval, in which the seismo-

gram is used. The L1 norm emphasizes the high frequency of the data, whereas the L2 emphasizes the low frequency, as mentioned before. The error is defined as

$$e = \|f - M_0 g\|/(\|f\| * \|M_0 g\|)^{1/2}.   \quad (5)$$

The errors e_{L1} and e_{L2} are defined accordingly. We define the error

$$e_1 = (e_{L1} + e_{L2} + (2e_{L1}^2 + 2e_{L2}^2)^{1/2})/4   \quad (6)$$

to be the error estimation for one individual component. For one station, the error e_2 is defined the same way as e_1, except that the M_0 used in equation (5) is the average moment $(1/n \sum_{i=1}^{n} M_{0i})$ of all components used from the station. e_2 is a measure of the consistency of all components of one station, i.e., a minimum of e_2 gives closest ratios of different components, say SH/P_{nl}, of the synthetics to the data. In short, e_1 emphasizes the fit of individual components, whereas e_2 emphasizes the consistence of all components of one station. We defined the error form in equation (6) to consider the low- and high-frequency contents of the data equally, because no preference can be given to either frequency content in attempting broadband fits. We used the nonlinear part in equation (6) to avoid large scatters between e_{L1} and e_{L2}.

We go through the whole parameter space of θ, δ, and λ, conducting a grid search and at one point $(\theta_0, \delta_0,$

λ_0) we obtain the best source mechanism for n stations when

$$\frac{1}{n} \sum_{i=1}^{i=n} (e_{1i} + e_{2i}) \qquad (7)$$

reaches its minimum. The average of M_0 for all data used is the moment.

The complete parameter space Φ for source mechanisms is ($0 \leq \theta \leq 360°$, $0 \leq \delta \leq 90°$, $0 \leq \lambda \leq 360°$). Because one source mechanism can be described by two fault planes, the space of all possible source mechanisms should be smaller than Φ. A source mechanism can be described by the unit normal v of its fault plane and the unit slip vector u on it. If we define $b = u \times v$, then any two of these three vectors can describe the source mechanism uniquely. For a source mechanism, two fault planes exist. The relation between them is that u and v of one plane are v and u of the other. Thus, the given source mechanism can be represented either b or $-b$. Thus, we can chose one sign of $b \cdot e_z$ [e_z is unit vector of the vertical direction; downward is positive as used in Aki and Richards (p. 144, 1980)] to describe the whole parameter space. Using the formula of Aki and Richards (p. 115, 1980), we have

$$b \cdot e_z = \sin\delta \sin\lambda. \qquad (8)$$

Because $\sin\delta \geq 0$, we can use $-90 \leq \lambda \leq 90$ or $90 \leq \lambda \leq 270$, instead of $0 \leq \lambda \leq 360$. The space of all possible source mechanisms becomes ($0 \leq \theta \leq 360$, $0 \leq \delta \leq 90$, $90 \leq \lambda \leq 270$).

The space of the possible source mechanisms can be restricted further if there are P, SV, or SH polarity data available. The polarity data ($+$ or $-$) require that the final source mechanism gives the same polarity. The possible space would be one-eighth if P, SV, and SH polarities of one station are available. Including the polarity data as prior constraints makes our grid search code still shorter.

The search through the parameter space for the global minimum can be accomplished in two steps. The first run uses a coarse grid for θ, δ, λ and finds a minimum, and the next uses a finer grid around this minimum to get the global minimum.

The code takes 94 sec to find a minimum-error grid from the whole parameter space search, using a grid spacing of $10°$ on a SPARC II machine for one station (GSC long-period data of the Sierra Madre mainshock with the P and SH polarities). In this run, we used the vertical and radial components of P_{nl} waveforms (160 points in time series) and the vertical, radial, and tangential whole records (500 points). If more station data are available, the computer time is roughly the same, because the parameter space is reduced as a result of

more polarity data. It takes longer if the data are noisy when the first motion polarity is unclear.

Applications

In this section we discuss the application of this method to determine the source parameters of the four events introduced earlier, namely, Sierra Madre and Yucca Mountain sequences, along with the more distant Lee Vining event that occurred in the north (see Fig. 3). These events were chosen because other inversion studies have already been conducted on these mainshocks, and their results can be compared with those obtained from this new method. These comparisons are given in Figure 5. We use the same Green's functions as Dreger and Helmberger (1993, unpublished manuscript) to make these comparisons the most meaningful, i.e., a set of these fundamental Green's functions computed up to 5 hz by a frequency-wavenumber method for the SC model discussed earlier. In the following, we use the grid spacing of $5°$ that sample the depths, 5, 8, 11, and 14 km. The best-depth estimate is obtained from the depth that gives

Event	Information		Fault Planes $(\vartheta, \delta, \lambda)$	Plot	Axis	Moment
	Waveform	Polarity				
Sierra Madre (34.26,-118.00) 6/28/91 14:43:54	BB: GSC, ISA,PFO	GSC13 ISA1 PFO1 SBC13	(240,50,65) (96,46,117)		P(347,2) T(83,71)	$(2.3\pm0.6)\times10^{24}$
	LP3090		(235,50,65) (91,46,117)		P(342,2) T(78,71)	$(3.0\pm0.7)\times10^{24}$
Dreger&Helmberger,1991			(235,50,74)			2.5×10^{24}
Sierra Madre (34.25,-117.99) 6/28/91 17:0:56	BB: GSC, ISA,PFO	ISA1 PAS1 PFO1 SVD1	(245,55,55) (116,46,129)		P(359,4) T(96,62)	$(3.2\pm2.2)\times10^{22}$
	LP3090		(115,55,125) (244,46,51)		P(181,4) T(84,62)	$(2.1\pm0.5)\times10^{22}$
Yucca Mtn (36.70,-116.29) 6/29/92 10:14:22	BB: ISA, PAS,PFO SVD	GSC1 ISA1 PAS1 PFO13 SBC13 STA1 SVD1	(180,45,235) (45,55,300)		P(13,65) T(114,5)	$(3.0\pm1.3)\times10^{24}$
	LP3090		(180,45,235) (45,55,300)		P(13,65) T(114,5)	$(3.8\pm1.9)\times10^{24}$
Helmberger et al., 1992a			(178,48,241)			2.5×10^{24}
Yucca Mtn (36.70,-116.25) 6/29/92 10:31:2	BB: GSC, ISA,PAS	GSC1 ISA1 PAS1	(240,40,340) (346,77,232)		P(218,44) T(104,23)	$(6.9\pm1.9)\times10^{22}$
	LP3090		(259,67,333) (0,65,205)		P(219,35) T(310,2)	$(8.1\pm1.6)\times10^{22}$
Lee Vining (38.03,-119.07) 10/24/90 6:15:21	BB: PAS	GSC13 PAS13	(315,75,190) (222,80,345)		P(178,18) T(269,4)	$(1.3\pm0.3)\times10^{24}$
	LP3090		(135,85,215) (42,55,354)		P(4,28) T(263,20)	$(1.2\pm0.2)\times10^{24}$
Dreger&Helmberger 1993			(322,83,163)			9×10^{23}
Depolo&Horton,1991			Strike slip Strike 330			

Figure 5. Summary of the results and comparison with those of other studies. Information used for LP3090 is the same as that for BB. In the column of polarity, 1 stands for P, 2 for SV, and 3 for SH; in the column of axis, P is P axis, T is T axis. The unit for moment is dyne-centimeter.

the smallest error, as in the earlier study of Dreger and Helmberger (1993).

Sierra Madre Events

The Sierra Madre data are displayed in Figure 1. The body waves from the mainshock have been carefully

studied by Dreger and Helmberger (1991). They obtained a thrust mechanism with a strike of 235°, a dip of 50°, and a rake of 74° and a moment of 2.5×10^{24} dyn-cm. We will use a shorthand notation for these parameters, namely, (235, 50, 74). This solution is quite compatible with the teleseismic and strong motion data
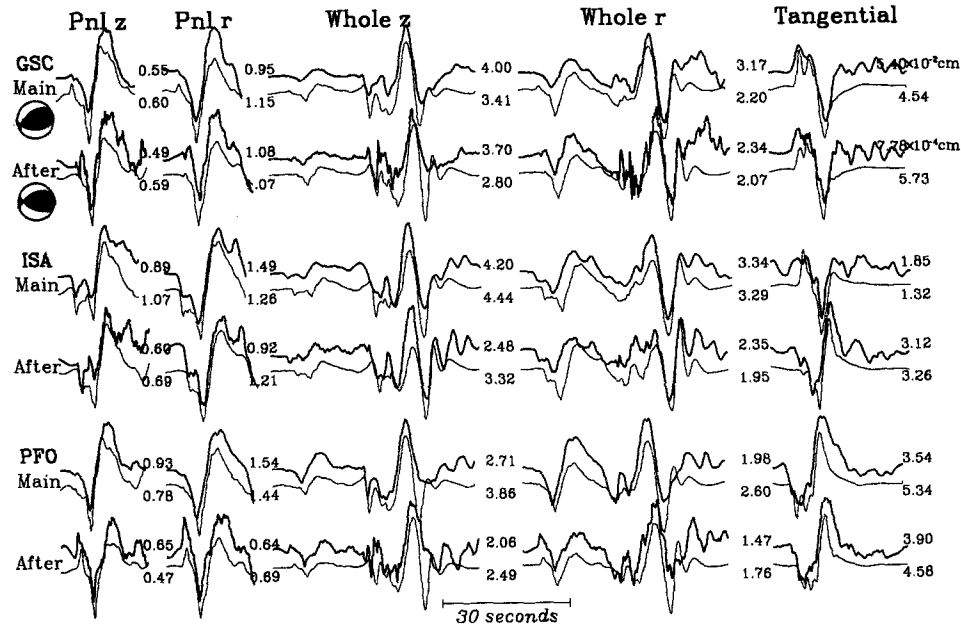
Figure 6.   Source mechanisms and synthetic predictions of the Sierra Madre mechanisms of mainshock and aftershock from broadband regional data bandpassed with Press–Ewing instrument response. The distance used for synthetics is 160 km for all stations, and the source depth is 11 km. The detailed information for the source mechanisms is given in Figure 5.
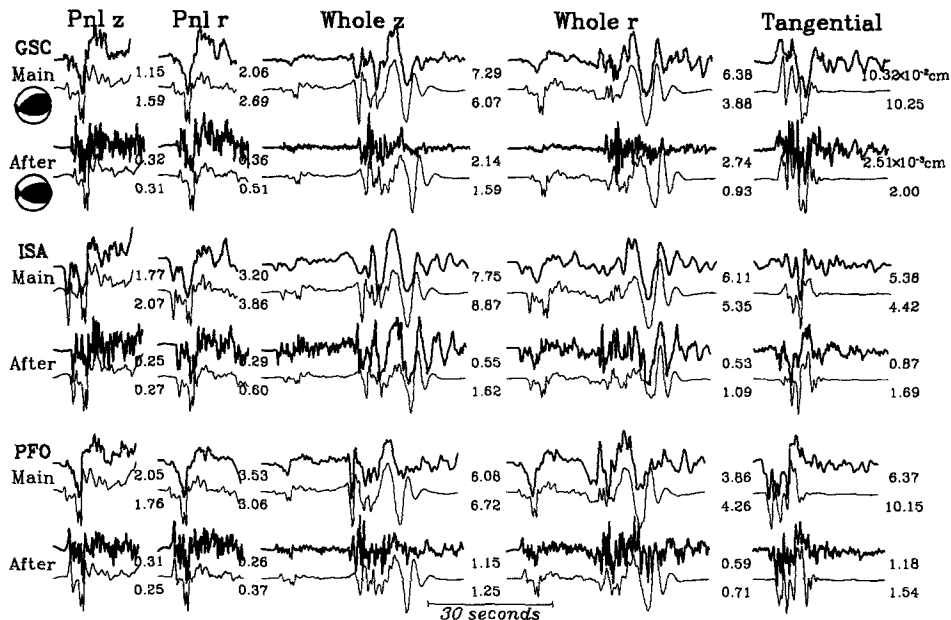

Figure 7.   Source mechanisms and synthetic predictions of the Sierra Madre mechanisms of mainshock and aftershock from broadband regional data.

(Wald 1992). We obtained two slightly different source mechanisms using broadband data and data bandpassed with a long-period Press–Ewing instrument response, see Figures 6 and 7. The source mechanism from broadband data is (240, 50, 65), and the moment is (2.3 ± 0.6) × 10^{24} dyn-cm; that from long-period bandpassed data is (235, 50, 65), and the moment is (3.0 ± 0.7) × 10^{24}

dyn-cm. The source function was determined by Dreger and Helmberger (1991) to be a (0.5, 0.5) triangle by modeling direct S at Pasadena. We find that adding some longer period, namely (0.3, 0.4, 0.3), produced a better fit at these more distant stations. As shown in Figure 5, the agreement in mechanisms between these methods is excellent. We used six polarities available from four sta-
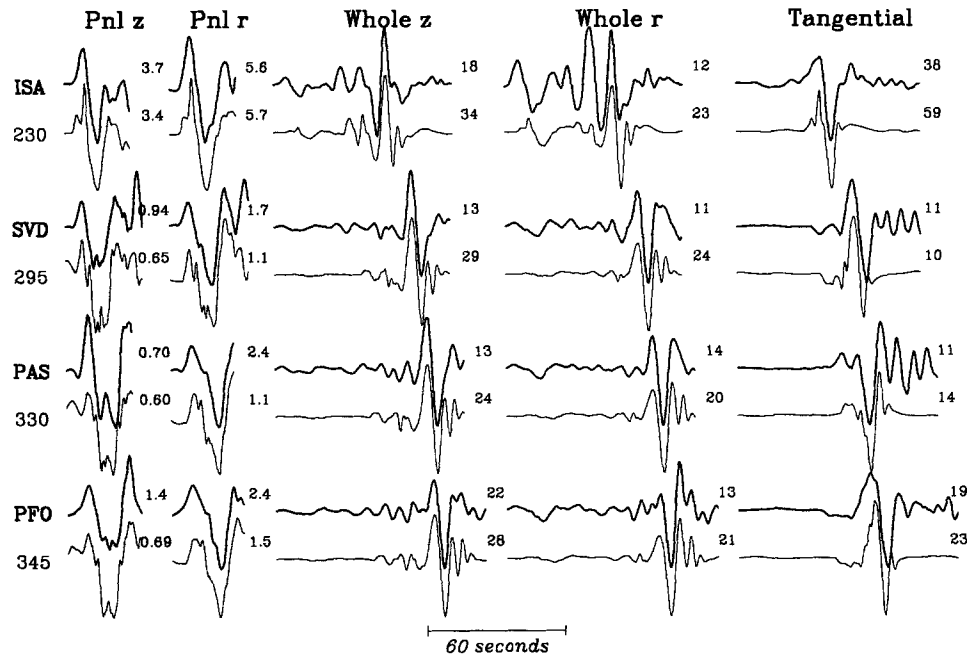
Figure 8. Long-period data and synthetic predictions of the Yucca Mountain mainshock.
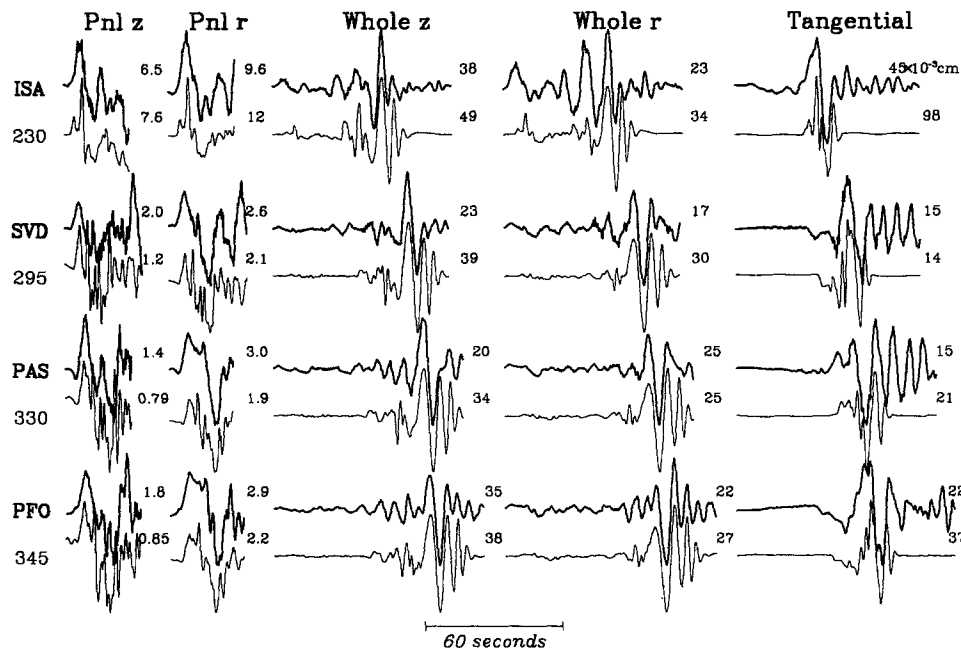
Figure 9. Broadband data and synthetic predictions of the Yucca Mountain mainshock.

tions, i.e., the P and SH polarities of GSC and SBC stations and the P polarities of ISA and PFO stations before constrain the parameter search. Note that the moment estimates from the long-period data are probably more accurate because the broadband is sensitive to asperity content. As discussed by Dreger and Helmberger (unpublished manuscript), the shorter the period the smaller the moment required to model the data.

For the aftershock, the broadband data show greater high-frequency content (Fig. 7). The polarities of SH are unclear for all the stations, but the polarities of P are clear at the stations GSC, PAS, PFO, and SVD. The source mechanism obtained from broadband waveforms is (245, 55, 55), and the moment is $(3.2 \pm 2.2) \times 10^{22}$ dyn-cm. The source mechanism of (244, 48, 51) and the moment of $(2.1 \pm 0.5) \times 10^{22}$ dyn-cm are obtained from long-period bandpassed waveforms. The source function obtained is (0.2, 0.3, 0.2). The source depth, 8 km, is
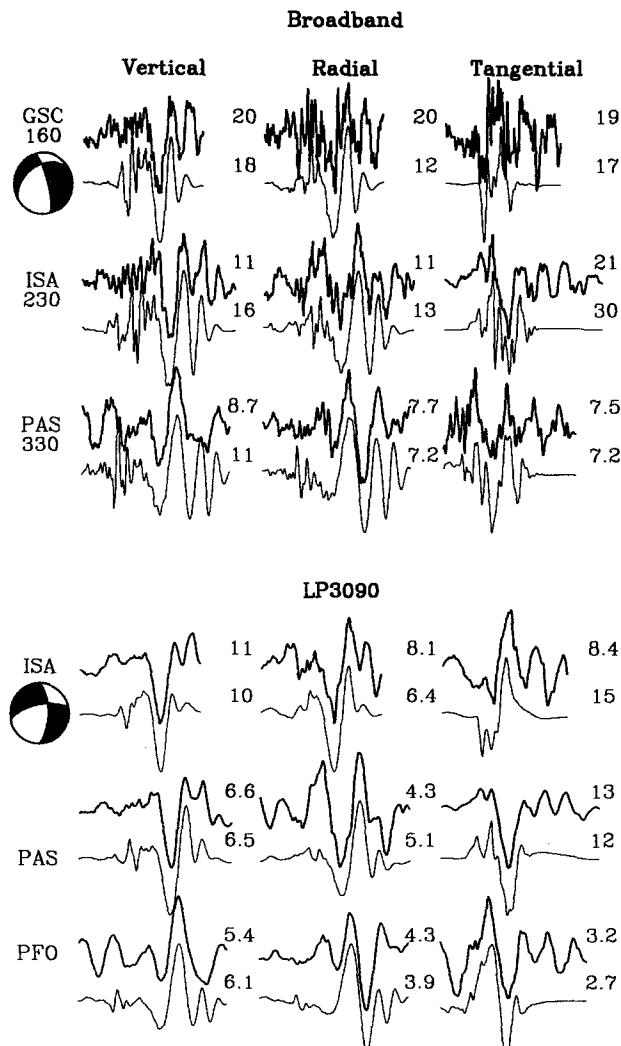

Figure 10.   Broadband and long-period data and synthetic comparison of the Yucca Mountain aftershock. The numbers beneath the station names are the distances of synthetics used.

determined from the comparison with 5 and 11 km. The reason for the large scatter of the moment estimate from the broadband waveforms is that the Green's functions are not good up to the frequency content of the data. In this case, the source estimation from long-period data should be better.

Although the source mechanism of the mainshock is not much different from that of the aftershock, they certainly produce very different waveforms at certain stations (see, e.g., the tangential components of ISA station and the vertical and radial components of P_{nl} waveforms at PFO station). An overlay to the long-period waveforms from these two events reveals that the separation between the P_{nl} and Rayleigh waves is slightly larger for the aftershock than for the mainshock. The code finds the largest shift at GSC to be about 2 sec. The best fit for the aftershock occurs for the 8-km depth Green's functions as opposed to 11 km for the mainshock. Given these discrepancies, it appears that more fine tuning in depths is warranted in that the main event probably needs to move upward and the aftershock downward. This type of precision will be investigated in future studies.

Yucca Mountain Events

The Yucca Mountain events occurred about 250 km NE of the network (see Fig. 3). The mainevent had a magnitude of 5.5 and occurred in Nevada at 36.6°N, 116.3°E, (NEIC). Figures 8 and 9 display the waveform data along with the best-fitting synthetics for a normal fault (see Fig. 5). The P polarities were mostly positive except at PAS where P_n is slightly negative. The SH polarities show a definite change between stations SVD and PAS, which strongly constrains the strike. The broadband and long-period waveform data yield a consistent mechanism of (180, 45, 235) with a moment estimate of 3.0 and 3.8×10^{24} dyne-cm. These results are quite compatible with regional P_{nl} and teleseismic body-wave
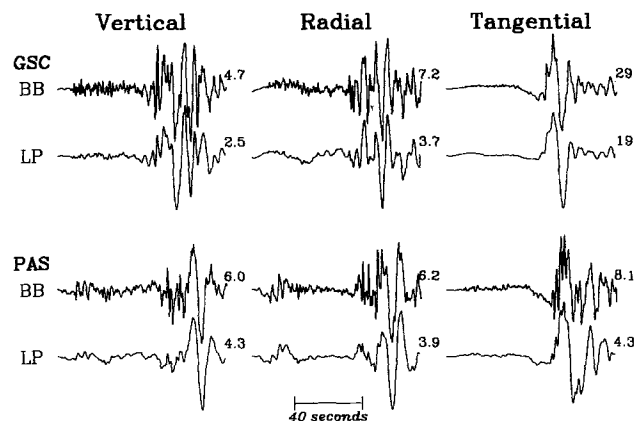

Figure 11.   Broadband and bandpassed (long-period Press–Ewing) data of the Lee Vining earthquake. The amplitudes are in 10^{-3} cm.

data (Helmberger *et al.*, 1992). The preferred depth was 11 km with the assumed time history of the (1, 1) triangle. Better Green's functions would be needed to justify extracting much more information. The inadequacy of the Green's functions is quite apparent in the shifts required for alignment. For example, the P_{nl}s have been lagged by 2.8 sec on average, whereas the Rayleigh waves required over 8 sec and Love waves 4 sec. Thus, the crust must be slowed down and thicken than the model in accordance with Braile *et al.* (1989). A thicker crust tends to produce longer period surface waves along with reduced peak amplitudes. This effect would also help explain the obvious discrepancies in M_0 estimation suggested in Figure 9 between P_{nl} and *SH* waves.

The results for the aftershock are displayed in Figure 10 where only the surface waves are above the noise, as discussed earlier. From the short-period bandpass of the data, we get three clear *P* polarities from GSC, ISA, and PAS. Using the dataset available, we obtained a source mechanism of (240, 40, 340) and a moment of (6.9 ± 1.9) × 10²² from broadband data and a somewhat different mechanism of (259, 67, 333) and a moment of (8.1 ± 1.6) × 10²² dyne-cm from long-period data. Figure 10 shows the comparison of synthetics to both broadband and long-period data. The source depth is determined at 11 km, and the source function is (0.3, 0.2, 0.3). As discussed above for the mainshock, the moment obtained here for the aftershock could be smaller, because the data used are surface wave only.

Lee Vining Event

For this event, data from only two stations, GSC and PAS, are available. The station azimuths differ by only 15° (Fig. 3). The data are displayed in Figure 11. Be-
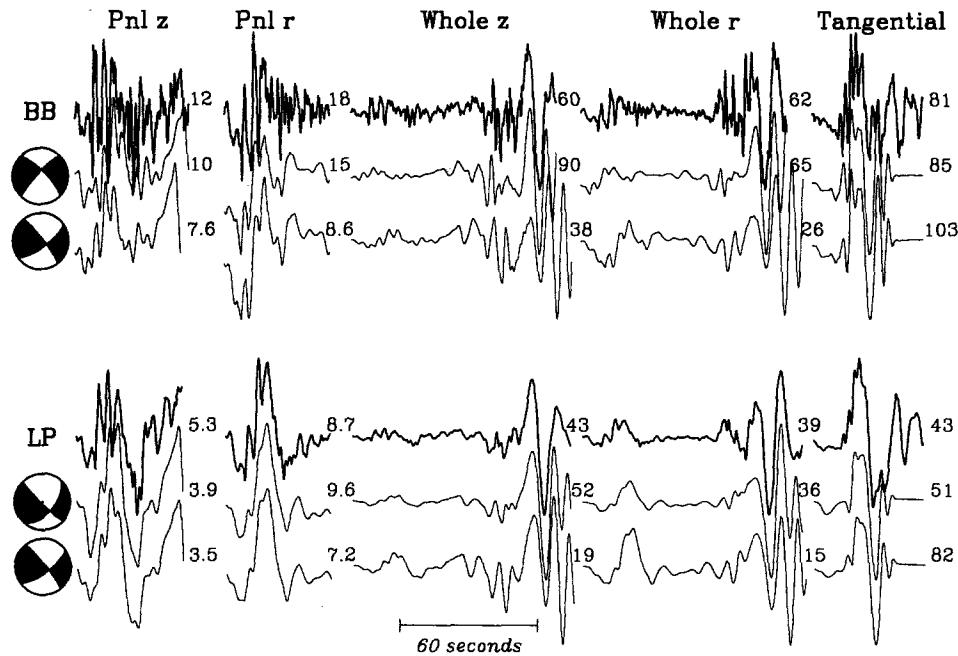

Figure 12. Source mechanisms, data, and synthetic comparisons of the Lee Vining event. In each group, the top trace is the data, the middle is the synthetics predicted by the source mechanism obtained in this study (Figure 5), and the bottom trace is the synthetics predicted by the source mechanism given by Dreger and Helmberger (1993). The amplitudes are in 10^{-4} cm.

Table 3
Models

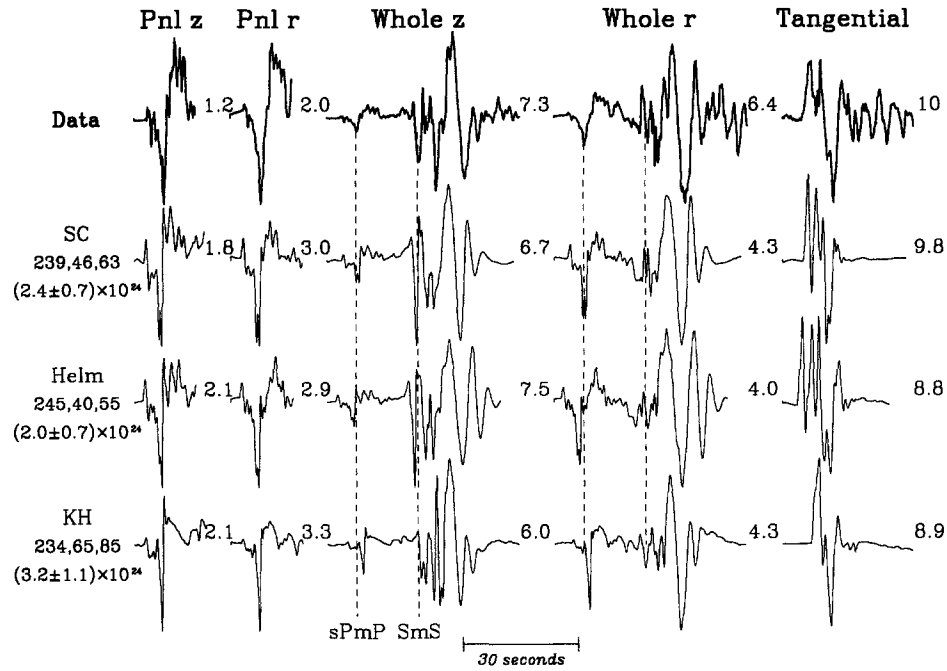| SC				Helm				KH				JD			
α	β	ρ	Thick	α	β	ρ	Thick	α	β	ρ	Thick	α	β	ρ	Thick
5.50	3.18	2.40	5.5	5.50	3.00	2.40	5.5	5.50	3.18	2.40	4.0	5.10	3.02	2.50	2.0
6.30	3.64	2.67	10.5	6.30	3.60	2.60	9.5	6.30	3.60	2.60	22.0	5.80	3.45	2.65	6.0
6.60	3.87	2.80	19.0	6.70	3.80	2.80	19.0	6.80	3.90	2.80	6.0	6.20	3.65	2.73	14.0
7.80	4.50	3.10	—	7.80	4.30	3.32	—	7.80	4.50	3.30	—	6.90	3.85	2.90	14.0
												7.90	4.40	3.21	—

Figure 13.   GSC recordings of the Sierra Madre event and the synthetics of the corresponding source mechanisms obtained from the source estimation code of this study for different models. On the left of the synthetics are the model, the source mechanism (strike, dip, slip), and the moment obtained in dyne-centimeters. SC stands for Southern California model, from Dreger and Helmberger (1991); Helm is from Helmberger et al. (unpublished manuscript) and KH is a model for Mojave desert (Kanamori and Hadley, 1975). The amplitudes are given on the right of the seismograms, the unit is in 10^{-2} cm.
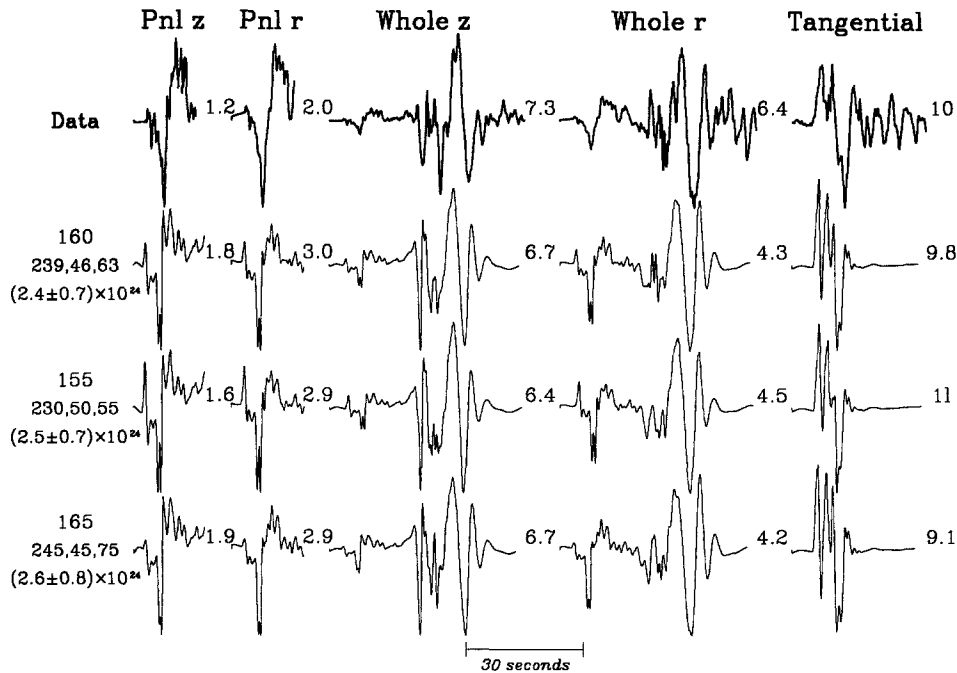

Figure 14.   Source mechanisms and data synthetic comparisons for different distances. The left of the seismograms gives the distance, the source mechanism, and the moment obtained. The data used are the GSC recordings of the Sierra Madre mainshock. The amplitude scale is 10^{-2} cm.
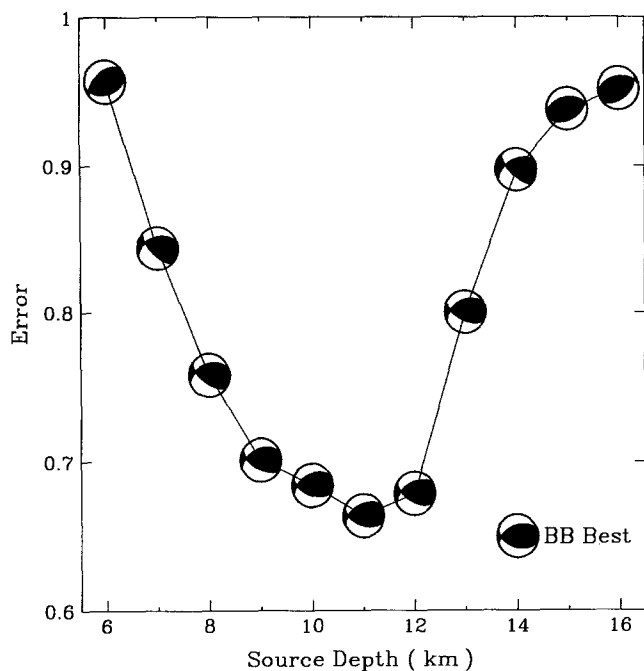
Figure 15. Error plots as a function of source depth. The source mechanisms are the source mechanisms obtained for the corresponding depths. The data used is the GSC records of the Sierra Madre mainshock. The source mechanism at the bottom left corner is the best source mechanism from all broadband data, as displayed in Figure 5.

cause the P_{nl} portion of the data is close to nodal and the Rayleigh waves are complicated at station GSC, we did not use the GSC waveforms but explored the single-station solution at PAS. The model SC is not likely to be a good model for the paths, because it is quite different from the model JD derived especially for the paths by Jones and Dollar (1986; Table 3). We will return to this model later. Figure 12 gives the synthetic comparisons of the source mechanisms obtained in this study along with that of Dreger and Helmberger (1993) for both the broadband and long-period data. The source mechanism (315, 75, 190) and moment $(1.3 \pm 0.3) \times 10^{22}$ dyn-cm obtained from the broadband data differ slightly from source mechanism (315, 95, 145) and moment $(1.2 \pm 0.2) \times 10^{22}$ dyn-cm obtained from the long-period data (Figs. 5 and 12). Both source mechanisms agree with those of Dreger and Helmberger (1993) and Depolo and Horton (1991) from first motion data. The depth is 11 km, and source function is (1, 1, 1).

Changes in the model can have a significant effect on the mechanism if only the body waves are used. For example, the use of model JD in Table 3 (Jones and Dollar, 1986) produced a 30° shift in rake relative to model SC (Dreger and Helmberger, 1993). This does not occur when the complete records are used. Thus, it appears that a single station can yield quite good results when the fits are adequate. We will explore this issue in the

next section along with a discussion of what features control the mechanisms and the moment.

Discussion

In the last section, we emphasized the comparison of our solutions with previous results with less emphasis on waveform stability as function of depth, range, and crustal model. These sensitivity issues become particularly important when the data become sparse. This is the situation when we study historic events where only one or two long-period seismograms are available. To gain experience in what one can expect from one-station inversions, we will look again at the data from the Sierra Madre event and compare the results using one station at a time.

We begin with some sensitivity considerations involving only station GSC as displayed in Figures 13, 14, 15, and 16. The model sensitivity is investigated to some extent in Figure 13. Two new models are introduced, namely, Helm (Helmberger *et al.*, unpublished manuscript) and KH (Kanamori and Hadley, 1975; see Table 3). Model Helm is similar to SC except that the shear velocities were reduced. This feature provides better fits to the *SH* waveforms and develops the Rayleigh wave dispersion. Model KH is generally faster and sharpens the Rayleigh waves, resulting in inferior fits, although the estimated mechanism is not very far off.

The range sensitivity is displayed in Figure 14 where the presence of P_mP and sP_mP add some high-frequency changes to the P_{nl} portion, see Helmberger *et al.* (unpublished manuscript). These small changes in range do not change the source estimation very much.

An example of depth sensitivity is displayed in Figure 15 where the mechanism is used as a plotting symbol. Obviously, the minimum error is reached at the depth of 11 km. Clearly, the source mechanisms are very similar in a wide range of depths around the depth with the minimum error. In Figure 16, the broadband results using three different depths are displayed, namely, 11, 8, and 14 km. The synthetics for the depth of 8 km show enhanced Rayleigh waves relative to the other two depths and look similar to the data, especially on the radial component. The P_{nl} waveforms for this depth do not fit quite as well. Synthetics for the depth of 14 km do not fit nearly as well as those provided by the other two depths and the mechanism begins to wander. The depth dependence on moment is expected because the shallow Green's functions become stronger for a fixed moment.

As mentioned earlier, we want to apply this method to sparse datasets, either isolated broadband station recordings of modern events or older analog station recordings of historic events. Figure 17 displays the source estimates again at GSC where we have included the long-period Wood–Anderson simulations, WALP. This response is similar to that of many older instruments (see

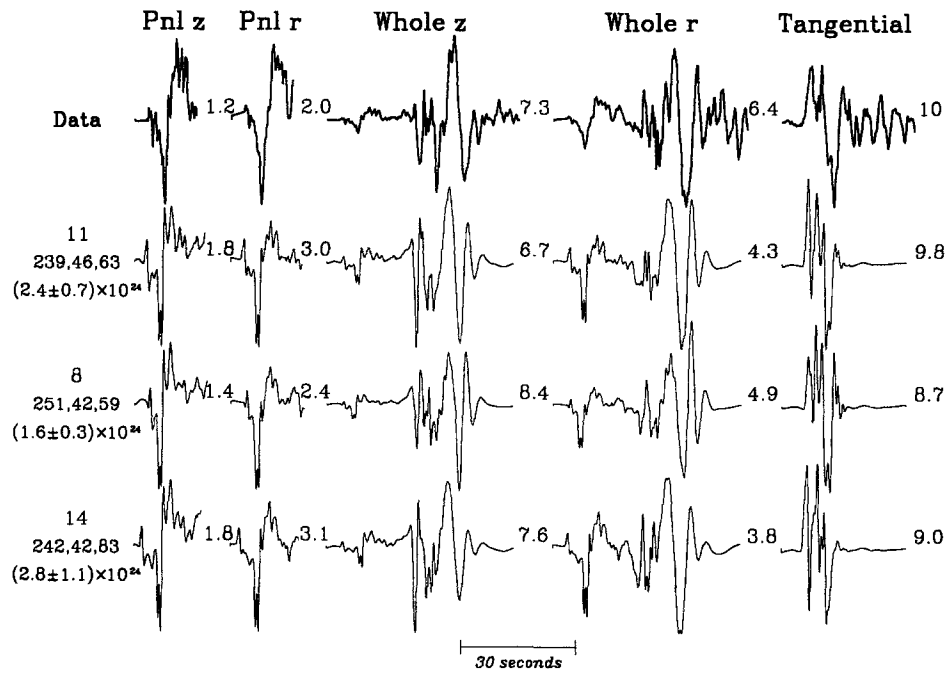Pnl z   Pnl r   Whole z   Whole r   Tangential

Figure 16.   Data and synthetic comparisons for different source depths. The
left side of the seismograms gives the depth, the source mechanism, and the
moment obtained. The data used are the GSC recordings of the Sierra Madre
mainshock. The amplitude scale is 10^{-2} cm.

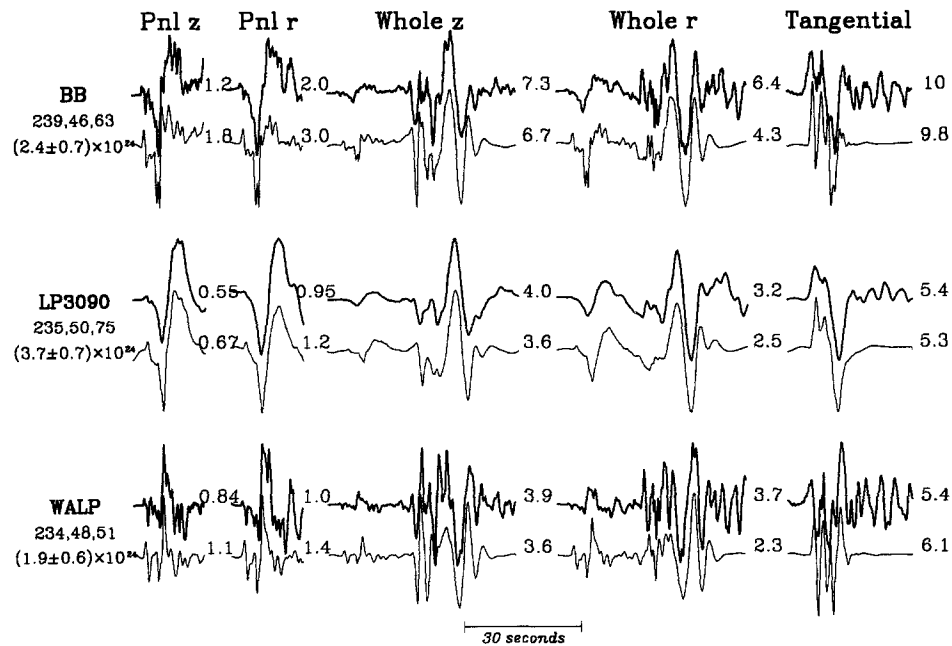Pnl z   Pnl r   Whole z   Whole r   Tangential

Figure 17.   Data and synthetic comparisons for the source mechanisms ob-
tained from different bandpasses. The left of the seismograms gives the filter,
the source mechanism, and the moment obtained. The data used are the GSC
recordings of the Sierra Madre mainshock. The amplitude scale is 10^{-2} cm. The
gain used is one for both LP3090 and WALP (Wood–Anderson long-period).

| Information | Fault Planes | | | | |
Station	Polarity	$(\vartheta, \delta, \lambda)$	Plot	Axis	Moment
BEST		(235,50,65) (91,46,117)		P(342,2) T(78,71)	$(3.0\pm0.7)\times10^{24}$
GSC(BB)	P, SH	(239,46,63) (95,50,115)		P(168,2) T(71,71)	$(2.4\pm0.7)\times10^{24}$
GSC(LP)	P,SH	(235,50,75) (78,42,107)		P(336,4) T(84,78)	$(3.7\pm0.7)\times10^{24}$
GSC(WA)	P, SH	(234,48,51) (105,55,125)		P(171,5) T(74,62)	$(1.9\pm0.6)\times10^{24}$
ISA(BB)	P	(237,38,54) (100,60,115)		P(172,12) T(56,65)	$(2.2\pm0.2)\times10^{24}$
ISA(LP)	P	(226,45,45) (100,60,125)		P(166,9) T(61,59)	$(2.9\pm0.4)\times10^{24}$
ISA(WA)	P	(230,60,55) (105,45,135)		P(345,8) T(69,59)	$(2.2\pm0.3)\times10^{24}$
PFO(BB)	P	(245,60,90) (65,30,90)		P(335,15) T(155,75)	$(2.1\pm0.4)\times10^{24}$
PFO(LP)	P	(199,64,46) (85,50,145)		P(319,8) T(59,50)	$(2.4\pm0.5)\times10^{24}$
PFO(WA)	P	(245,65,105) (33,29,61)		P(324,19) T(182,67)	$(1.8\pm1.1)\times10^{24}$

Figure 18. Single station estimates. LP is Press–Ewing. WA is long-period Wood–Anderson.

| | Fault Planes | | | |
Information	$(\vartheta, \delta, \lambda)$	Plot	Axis	Moment
BEST	(235,50,65) (91,46,117)		P(342,2) T(78,71)	$(3.0\pm0.7)\times10^{24}$
Pnl only	(240,50,90) (60,40,90)		P(330,5) T(150,85)	$(3.0\pm0.3)\times10^{24}$
Rayleigh	(235,50,50) (108,54,127)		P(172,2) T(78,60)	$(3.1\pm0.5)\times10^{24}$
SH only	(214,78,36) (115,55,165)		P(340,15) T(81,34)	$(2.1\pm0.5)\times10^{24}$
Whole	(221,52,63) (81,45,120)		P(330,4) T(69,69)	$(3.1\pm0.9)\times10^{24}$
Pnl + Sn	(245,55,100) (48,36,76)		P(328,9) T(189,77)	$(3.4\pm1.1)\times10^{24}$
Pnl + SH	(235,55,65) (94,42,121)		P(342,7) T(90,69)	$(3.0\pm0.5)\times10^{24}$
Pnl + Rayl	(237,50,67) (90,45,115)		P(343,3) T(81,72)	$(3.0\pm0.6)\times10^{24}$
Pnl + Whole	(232,50,67) (85,45,115)		P(338,3) T(76,72)	$(3.0\pm0.6)\times10^{24}$
Rayl + SH	(230,55,60) (95,45,126)		P(341,6) T(83,65)	$(3.0\pm0.8)\times10^{24}$
Whole + SH	(233,48,59) (95,50,120)		P(164,1) T(71,67)	$(3.0\pm0.6)\times10^{24}$

Figure 19. Information search. Whole means the whole waveforms of vertical and radial components; Rayl(eigh) means the waveforms from *Sn* arrival. The data used are bandpassed with Press–Ewing instrument response.

e.g., Helmberger *et al.*, 1992b). Because their gains are relatively low, they provide excellent data for examining larger historic events. A comparison of the source estimates from these three responses as a function of station is given in Figure 18. The results are quite encouraging and could probably be improved by filtering the higher frequencies in the WALP response, especially for moment estimation.

The ability to estimate the source properties with one station suggests that there must be a great deal of redundancy in the entire network. We attempt to address this issue by generating solutions from various portions of the three Sierra Madre records (GSC, ISA, and PFO). The results are given in Figure 19. In general, any two sets, P_{nl} and *SH*, P_{nl} and Rayleigh, or *SH* and Rayleigh do well. Using only P_{nl} or Rayleigh (note that Rayleigh also contains *SV*) produces reasonable results, whereas SH alone does the poorest, as it should theoretically. The relative amplitudes between stations become particularly important in this case and could probably be improved with receiver function corrections.

Conclusions

We presented a new method of estimating source parameters based on the waveforms and amplitudes of regional seismograms. The seismograms are decomposed into segments containing body waves and surface

waves that are fitted separately with the use of a direct grid search procedure. Because we need not require smooth derivatives, we can use broadband data with any measure of fit deemed interesting. In this application, we used a linear average of L1 and L2 norms. We found that one-station solutions prove quite effective in many situations, especially with some additional constraints provided by other short-period polarities. Thus, this technique is ideally suited for studying historic events if some form of long-period records are available. Moreover, because the choice of a regional model is not very crucial, we can use this technique for rapid determination of source parameters with arrays such as TERRAscope.

Acknowledgments

tion No. 5245, Division of Geological and Planetary Sciences, California Institute of Technology, Pasadena, California.

References

Aki, K. and P. G. Richards (1980). *Quantitative Seismology: Theory and Methods*, W. H. Freeman, San Francisco, California.

Braile, L. W., W. J. Hinze, R. R. B. von Frese, and G. R. Keller (1989). Seismic properties of the crust and uppermost mantle of the conterminous United States and adjacent Canada, in *Geophysical Framework of the Continental United States, Geological Society of America Memoir* **172**, L. C. Pakiser and W. D. Mooney (Editors), Geological Society of America, Boulder, Colorado, 655–679.

Depolo, D. M. and S. P. Horton (1991). A magnitude 5.0 earthquake near Mono Lake, California, *Seism. Res. Lett.* **62**, 52.

Dreger, D. S. and D. V. Helmberger (1991). Source parameters of the Sierra Madre earthquake from regional and local body waves, *Geophys. Res. Lett.* **18**, 2015–2018.

Dreger, D. S. and D. V. Helmberger (1993). Determination of source parameters at regional distances with three-component sparse network data, *J. Geophys. Res.* (in press).

Helmberger, D. V. (1983). Theory and application of synthetic seismograms, in *Proceedings of the International School of Physics «Enrico Fermi», Course LXXXV, Earthquakes: Observation, Theory and Interpretation*, H. Kanamori and E. Boshi (Editors), North-Holland, Amsterdam.

Helmberger, D., P. Somerville, and E. Garnero (1992b). The location

and source parameters of the Lompoc, California Earthquake of 4 November 1927, *Bull. Seism. Soc. Am.* **82**, 1678–1709.

Helmberger, D., L. Zhao, and D. Dreger (1992). Source estimation from regional seismograms, in *Proc. of the 14th Annual PL/DARPA Seismic Res. Symp.* 16–18 September 1992, Tucson, Arizona, 173–179.

Jones, L. M. and R. S. Dollar (1986). Evidence of Basin-and-Range extensional tectonics in the Sierra Nevada: The Durwood Meadows Swarm, Tulare County, California (1983–1984), *Bull. Seism. Soc. Am.* **76**, 439–461.

Kanamori, H. and D. Hadley (1975). Crustal structure and temporal velocity change in southern California, *Pure Appl. Geophys.* **113**, 257–280.

Kanamori, H., E. Hauksson, and T. Heaton (1992). TERRAscope, *Eos Trans. AGU* **73(43)**, Fall Meeting Suppl., 371.

Thio, H. K. and H. Kanamori (1992). Moment tensor inversions in Southern California using surface waves recorded by TERRAscope, *Eos Trans. AGU* **73(43)**, Fall Meeting Suppl., 376.

Wald, D. (1992). Strong motion and broadband teleseismic analysis of the 1991 Sierra Madre, California earthquake, *J. Geophys. Res.* **97**, 11033–11046.

Zhao, L. S. and D. V. Helmberger (1991). Broadband modeling along a shield path, Harvard recording of the Saguenay earthquake. *Geophys. J. Int.* **105**, 301–312.

Seismological Laboratory
California Institute of Technology
Pasadena, California 91125